Carbon 170 (2020) 452–463

Contents lists available at ScienceDirect

Carbon

journal homepage: www.elsevier.com/locate/carbon

Research Article

Synthesis and growth mechanism of bamboo like *N*-doped CNT/Graphene nanostructure incorporated with hybrid metal nanoparticles for overall water splitting

Anchu Ashok [a], Anand Kumar [a, *], Janarthanan Ponraj [b], Said A. Mansour [b]

[a] Department of Chemical Engineering, College of Engineering, Qatar University, P O Box – 2713, Doha, Qatar
[b] Qatar Environment and Energy Research Institute (QEERI), Hamad Bin Khalifa University, Qatar Foundation, PO Box 34110, Doha, Qatar

ARTICLE INFO

Article history:
Received 18 June 2020
Received in revised form
15 August 2020
Accepted 17 August 2020
Available online 24 August 2020

Keywords:
Hydrogen evolution reaction (HER)
Oxygen evolution reaction (OER)
Overall water splitting

ABSTRACT

Herein, we report a melamine and metal-salt based pyrolysis technique for synthesizing metal encapsulated *N*-doped carbon nanotube (CNTs) in form of bamboo-like CNTs and multi walled CNTs (MWCNT). Sulfur doping during synthesis greatly influenced the physio-chemical properties of the material formed. X-ray diffraction (XRD) analysis confirms NiCo alloy (NiCo@CNT) formation that transformed into a hybrid $NiCo/Co_3Ni_6S_8/Co_3O_4$ nanocomposite (NiCoS@CNT) in presence of sulfur. A detailed study was conducted on the mechanism of the formation of metal-encapsulated *N*-doped CNT structures from the polymerization of melamine. The unique NiCoS@CNT structure renders high specific surface area (232.2 m^2/g), large pore volume (0.92 cm^2/g), and high lattice defect with abundant oxygen vacancies resulting in excellent performance for OER and HER in alkaline medium. The hybrid catalyst requires over-potentials of 198 mV and 295 mV to deliver a current-density of 10 $mAcm^{-2}$, respectively for HER and OER. A cell voltage of only 1.53 V was required to deliver a long-term stable current-density of 10 $mAcm^{-2}$ for water splitting when NiCoS@CNT was used as both anode and cathode. Superior performance of NiCoS@CNT could be ascribed to high surface area, abundant active sites, fast charge-transfer rate, high pyridinic-N content and the presence of highly conductive CNT architecture.

1. Introduction

As the world advances, the demand for energy consumption also increases. Electricity, the primary driver of the economy of the world, is mainly obtained by the burning of fossil fuels. This gives rise to a large scale emission of greenhouse gases into the atmosphere which in turn results in global warming [1,2]. An alternative method, which is environmentally friendly, clean and, economically efficient, is in great demand for the production of electricity. During the last few decades, there has been a wide range of studies targeting the conversion of renewable energies; such as solar energy, wind energy, blue energy, etc. Into electricity. The basic challenge with the renewable energy sources is that they are intermittent and require an economical and efficient storage solutions for uninterrupted delivery. Water splitting is considered as a sustainable method to convert such energies into the form of chemical fuels (i.e. hydrogen and oxygen) with no carbon emission that can then be stored and used later as desired [3,4].

Two half-reactions, oxygen evolution reaction (OER) at the anode and hydrogen evolution reaction (HER) at the cathode, occur during the water splitting. Hydrogen and oxygen, produced during the HER and OER respectively, find many applications in our growing industries. Hydrogen has been deemed a promising energy carrier with zero carbon content to satisfy our need for potential fuel applications [5,6]. Hence, the production of hydrogen by water splitting has been of great demand over the last few decades, nonetheless, some challenges persists before starting a large-scale production plant. The theoretical thermodynamic potential for overall water splitting is about 1.23 V, however, the commercial water electrolyzer need more potential because of the high overpotential required in presence of available catalysts and sluggish reaction kinetics of OER and HER [7–13]. Therefore we need an efficient electrocatalyst to reduce the overpotential and accelerate the hydrogen and oxygen production, with high stability, in a wide range of pH to be of any practical significance. Generally, Ru and Ir based oxides (i.e. RuO_x and IrO_x) are reported to be effective

* Corresponding author.
E-mail address: akumar@qu.edu.qa (A. Kumar).

https://doi.org/10.1016/j.carbon.2020.08.047

catalysts for OER [14–16]. Whereas for HER, Pt-based catalysts show high activity and stability in acidic medium. For large scale applications, these electrocatalysts would result in excessive cost for hydrogen production due to the scarcity of these elements; in addition to the challenges associated with the compatibility of Pt and Ru/Ir with each other in a single electrolytic system. As a result, extensive studies have been performed by researchers to find alternative electrocatalysts that are effective in terms of cost, availability, activity and stability, that can work at a wide range of pH value. To improve the activity of electrocatalysts, many methodologies have been explored that include: increasing the active site centers, improving conductivity by doping with conductive elements, modulating the electronic structure, creating vacancies, altering the morphology, providing support, etc [17,18]. Recently, transition metals in various forms have gained attention as bifunctional catalysts towards overall water splitting. Transition metal oxides, layered double hydroxides (LDH), chalcogenides, nitrides, carbides, perovskites, etc. have been found to be of particular research interest [19–23].

The inclusion of more abundant transition metals, such as nickel or cobalt, to form nickel and cobalt-based sulfide catalysts showed excellent activity towards overall water splitting [24–26]. Wenxin Zhu et al. grew a microsphere film of NiS on nickel foam (NiS/NF) through a sulfurization reaction, resulting in a Janus catalyst that delivered 158 mV overpotential for HER at 20 mA cm^{-2} and 335 mV overpotential at 50 mA cm^{-2} for OER under 1 M KOH electrolyte [27]. The bifunctional electrode showcased 1.64 V towards overall water splitting at 10 mA cm^{-2} current density which can be applied on a large-scale hydrogen production. Changing the electronic structure by doping with other elements have been found to increase the activity of the electrocatalyst significantly. In a different study, the same team fabricated bimetallic Fe-Ni sulfide nanowall arrays supported on a foam of nickel (Fe11.1%-Ni_3S_2/NF) through wet chemistry topotactic conversion from its LDH precursor. Fe11.1%-Ni_3S_2/NF, under 1 M KOH, exhibited 1.60 V overall cell voltage to gain 10 mA cm^{-2} for overall water splitting [28]. During the same year, Geng Zhang and team studied the effect of Fe doping onto Ni_3S_2 which was vertically anchored on 3D NF. They found that the Fe addition significantly increased the electrochemically active surface area, conductivity and the water adsorption ability of the catalyst, which resulted in a low cell potential value of 1.54 V at 10 mA cm^{-2} as well as high durability [29]. Cobalt sulfide (Co_3S_4) shows high activity for HER in acidic media and for OER in alkaline media [30,31]. A hydrophilic 2D Co_3S_4 nanosheet bifunctional catalyst was synthesized by Mingchao Zhu and co-workers using hydrophilic solvent and precursors. An overall cell potential of 1.63 V at 10 mA cm^{-2} current density towards water splitting was observed [32]. Subhasis Shit et al. created cobalt sulfide-anchored nickel sulfide on a foam of nickel (CoS_x/Ni_3S_2@NF) via hydrothermal process, using NF as the nickel precursor. Due to the better charge transfer efficiency and a fall in the number of H^- and O^- species CoS_x/Ni_3S_2@NF showcased an exceedingly low cell voltage value of 1.573 V at 10 mA cm^{-2} [33].

In this work, we followed a single step cost effective pyrolysis technique for the synthesis of metal encapsulated carbon nanotube network by using melamine as the source of carbon and nitrogen. The metal nitrate not only acts as a source for the metal nanoparticle for encapsulation, it also acts as a catalytic active site for the formation of N doped carbon nanotubes with different alignments of graphene layer including bamboo CNT and multi walled CNT (MWCNT). Here in we propose a growth mechanism of the formation of bamboo like structure encapsulated with metal nanoparticle and g-C_3N_4 as intermediate on the basis of transmission electron microscopic analysis. We have shown the effect of the presence of sulfur during the synthesis that causes the formation of hybrid NiCo nanoparticle; whereas in absence of sulfur, the resulted metal phase was pure NiCo alloy. To the best of our knowledge, this is the first work on the formation of NiCo alloy and hybrid NiCo nanostructure embedded in a bamboo like CNT that have been used for the electrochemical HER and OER reaction.

2. Experimental procedure

2.1. Synthesis method

Typically, cobalt nitrate ($Co(NO_3)\cdot 6H_2O$, 0.5 g, 99.9%, Sigma Aldrich), nickel nitrate ($Ni(NO_3)\cdot 6H_2O$, 0.5 g, 99.9%, Sigma Aldrich), melamine (4 g, 99%, Sigma Aldrich) and thioacetamide (1 g, ≥99.0%, Sigma Aldrich) were mixed and finely ground using a hand motor for 10 min. The well mixed precursors were loaded in the quartz boat crucible that was placed inside a horizontal furnace to heat under continuous N_2 flow of 10 sccm at 900 °C for 2 h at a ramp of 4 °C/min. The black powder left over the crucible was measured to be 0.256 g. The obtained powder was washed alternately with DI water, ethanol and acetone in order to remove any impurities and dried under vacuum at 80 °C for overnight. The resulting powder was ground to obtain uniform particle and named it as NiCoS@CNT. To achieve the insight on the effect of sulfur doping in electrocatalytic activity and for comparative studies, NiCo@CNT without sulfur was also synthesized by following the same procedure in absence of thioamide.

2.2. Material characterization

Crystalline nature of the particles being synthesized were measured using a desktop X-ray powder diffractometer (XRD, Rigaku MiniFlexII) with Cu-Ka radiation of 0.154056 nm wavelength, within a scan range of 10–90°. HighScore Plus was used for the analysis of the XRD data and to identify the individual phases from the diffraction peaks. Scanning Electron Microscope (Nova Nano 450, FEI), with magnification of up to 200 kx coupled with EDX was used to identify the morphology and elemental composition. FEI Talos F200X TEM with an accelerating voltage 200 kV coupled with EDS (FEI SuperX EDS system) was used to analyze the particles size and shape and construct nanoscale phase mapping of the synthesized nanoparticles. X-Ray Photoelectron Spectroscopy (XPS, Kratos AXIS Ultra DLD) was utilized to understand the bonding configuration and surface elemental analysis. Calibration of XPS measurement was performed with respect to C 1s as standard. BET surface area and pore size analysis of the as-synthesized particles was measured using AimSizer (AS-3012). DXR Thermoscientific Raman spectrometer in the range of 10 cm^{-1} to 4000 cm^{-1} with a step size of 1.5 cm^{-1} and step time of 20 s at a wavelength of 514.53 nm was used for the detailed examination of carbon formed.

2.3. Electrochemical characterization

The electrochemical tests were performed using a 3-cell electrode system with PINE instrument biopotentiostat (Wave Driver 20) system at room temperature with 1 M KOH as an electrolyte medium. A Teflon supported 5 mm glassy carbon disc as working electrode, Pt coil and an Ag/AgCl (4 M saturated KCl) were used as counter and reference electrodes, respectively. Typically, the preparation of the working electrode was as follows: A 5 mg of catalyst was dispersed in 300 μl of isopropyl alcohol and 30 μl Nafion (as a binder), followed with 30 min sonication to achieve the homogeneity. Finally, a 5 μl of homogenous suspension was loaded over 5 mm glassy carbon electrode that was allowed to dry in air at room temperature. Initially, the working electrode is treated

electrochemically through a multiple oxidation/reduction cycles (100 cycles) in the potential window of 0.4 to −1 V at 500 mVs^{-1} scan rates in order to remove any impurities. The electrochemically stable cathode was further analyzed with the cyclic voltammetry (CV) in the same potential at 50 mVs^{-1} scan rates to understand the oxidation/reduction behavior of the catalysts. The polarization curves of catalysts were obtained using linear sweep voltammetry (LSV) at 5 mVs^{-1} scan rate. All potential reported here were converted into standard reversible hydrogen electrode (RHE) using the Nernst equation ($E_{RHE} = E_{Ag/AgCl} + 0.197 + 0.0591 \times pH$). Electrochemical impedance spectroscopy (EIS) was measured using Zahner Elektrik IM6 at different potentials with frequencies ranging from 0.1 Hz to 100 kHz and an amplitude of 5 mV. The electrochemical parameters of the EIS spectrum was extracted by fitting the EIS spectrum using Thales, Equivalent Circuit Simulation & Model Fit (SIM).

Overall water splitting: The overall water splitting experiment was conducted using NiCoS@CNT (or NiCo@CNT) loaded material as anode and cathode in 1 M KOH electrolyte. The electrolyte was purged with N_2 for 30 min before conducting the electrochemical analysis. The electrodes were prepared using a 1 cm × 3 cm carbon cloth that was pretreated alternately using HNO_3, ethanol and DI water a number of times in order to remove the contaminants. Typically, a 3 mg of catalyst was dispersed in a mixture of DI water (1 ml), iso-propyl alcohol (0.5 ml) and Nafion solution (0.03 ml) by sonication for 30 min. A 35 μl of thus prepared ink was dropped carefully over both the side of 1 cm × 1 cm portion of carbon cloth and allowed for drying in an oven kept at 40 °C. The fabricated electrode was used electrochemical purpose without any further treatment.

3. Results and discussion

3.1. Synthesis and characterization

XRD analysis of as-synthesized samples are shown in Fig. 1a. In NiCo@CNT profile, the broad peak at 26.1° corresponds to the crystal planes of (002) attributed to the presence of graphitic carbon arises from CNTs. Additional sharp peaks at 44.2°(111), 51.6°(200) and 75.9°(220) attributed to the existence of single phase NiCo alloy phase. While, the introduction of sulfur in NiCo completely changes the phases of the particles synthesized. NiCoS@CNT shows the existence of NiCo alloy as in NiCo@CNT sample, whereas other peaks at 15.4°, 29.7°, 31.1°, 39.4°,42.5°, 47.3°, 55.3°, 78.6° can be assigned to (111), (311), (222), (331), (422), (511), (442) and (733) crystal planes of $Co_3Ni_6S_8$. In short, NiCoS@CNT shows the presence of NiCo alloy and Co_3O_4 along with the significantly strong diffraction signals of $Co_3Ni_6S_8$, which confirms the successful impregnation of sulfur over NiCo lattice. The XRD analysis shows the presence of hybrid NiCo/$Co_3Ni_6S_8$/Co_3O_4 structure after the addition of sulfur into the lattice sites of NiCo. The average crystallite size for NiCo alloy at 44.2° using Scherer formula was calculated to be 44 nm for both samples, shows that there is no change in average particle size after sulfur doping. SEM images of as-synthesized material in Fig. 1b and c shows the presence of metal encapsulated carbon nanotubes that are tangled with each other in the length of several nanometer to micrometer range. A close investigation of some nanotubes shows the existence of bamboo like structure with the compartments of tube joined together.

EDX spectrum and corresponding elemental analysis (of the entire SEM area in Fig. 1b and c) presented in Fig. S1 reveals the presence of nickel and cobalt in 1:1 ratio, both, in presence and absence of sulfur. Moreover, the significant amount of nitrogen indicates that the carbon tubes formed were successfully doped with nitrogen during the synthesis. Noticeably, the atomic percentage of carbon in NiCo@CNT (96.43%) is higher than NiCoS@CNT (82.14). The presence of C and N was further confirmed using CHN analysis, where NiCo@CNT shows the C and N % to be 67.762% and 4.32% respectively and for NiCo@CNT the value was found to be 42.82% (C) and 3.93% (N). SEM-EDX and CHN analysis confirms the presence of more carbon content in the NiCo catalyst synthesized in

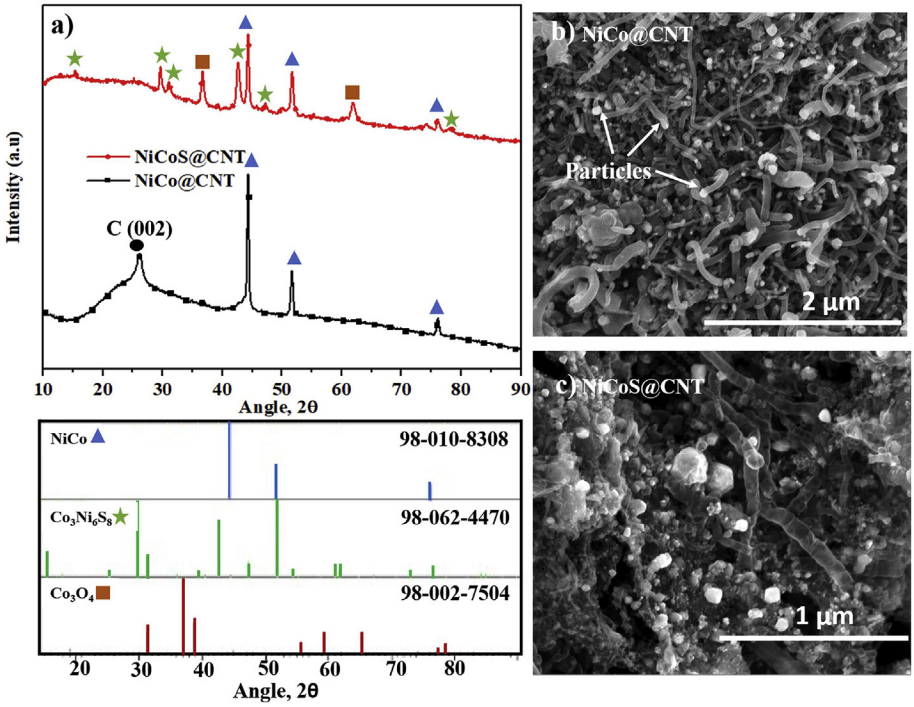

Fig. 1. a) XRD pattern of as-synthesized NiCo@CNT and NiCoS@CNT. SEM microimage of b) NiCo@CNT and c) NiCoS@CNT. (A colour version of this figure can be viewed online.)

absence of sulfur.

Raman spectroscopy of as-synthesized carbon rich samples was used to measure the degree of graphitization and disorderness of the sample. The broad peak around 648 cm^{-1} in NiCo@CNT attributed to the A_{ig} vibrational mode of NiCo alloy and the slight shift of the peak to 656 cm^{-1} in NiCoS@CNT could be due to the doping of sulfur in the NiCo lattice [34]. The two significant peaks in Raman spectrum for any carbon-based samples at approximately 1340 cm^{-1} and 1500 cm^{-1} correspond to the well-defined D and G band of carbon, respectively. The lattice defects in the carbon nanotube correspond to the D-band, whereas the G-band arise from the in-plane vibration of sp^2 carbon atoms, and the 2D peak (at 2690 cm^{-1} for NiCo@CNT) belongs to the double structure reference on the band structure of the graphene layer. The intensity ratio of D and G band (I_D/I_G) determines the degree of structural disorder in the carbon material, where higher the ratio indicates more defects [35,36]. Fig, 2a shows the raman spectrum of the as-synthesized sample. The I_D/I_G ratio for NiCo@CNT and NiCoS@CNT was measured to be 0.9182 and 0.757 respectively. The relatively strong 2D peak in NiCo@CNT shows the formation of a well crystalline graphene layer, whereas the weak 2D peak (almost completely suppressed) for NiCoS@CNT could be due to the large number of defects introduced into the graphene layer. It is worth mentioning that addition of sulfur in the reactive mixture during synthesis improves the surface defect and microstructural rearrangement of carbon atom in NiCoS@CNT, preferably due to the hybrid S and N atom doping on CNTs [8].

The porous nature and surface area of the produced sample was investigated using BET N_2 adsorption–desorption isotherms as in Fig. 2b. The specific surface area of NiCoS@CNT was found to be 232.2 m^2/g with 0.92 cm^2/g pore volume, while NiCo@CNT possess much lower surface area vale of 124.09 m^2/g having pore volume of 0.529 cm^2/g. Sulfur is introduced using thioacetamide (CH_3CSNH_2) as a precursor. During the thermal decomposition process leading to the synthesis of solid metal sulfides, other gaseous products such as CO_2, N_2, H_2O vapor etc. are also be released, which contribute towards furthering the porous nature of the solid as these gases form channels while escaping. Presence of thioacetamide in the synthesis mixture results in more gases during synthesis as compared to just the metal nitrate decomposition leading to NiCo synthesis, leading to higher surface area and more porosity (Fig. 2b and S2).

The pore size distribution profile (Fig. S2) shows the presence of pores in the size range of 1.5–2.5 nm for the two samples, right at the border of micro and mesoporous regions. The results also clearly depicts the role of sulfur doping during the synthesis to improve the surface area and pore volume to almost twofold, that could enhance the electrocatalytic properties of the synthesized materials. Generally, higher the surface area smaller the particle and shorter will be the electron diffusion length that can helps in expediting electron transfer during electrochemical reactions.

In-depth analysis on the morphology of particle formed in NiCo@CNT was conducted using transmission electron microscopy (TEM) as in Fig. 3. The TEM image reveal the presence of particles in the size of 10–50 nm incorporated on different form of carbons including graphene layer, bamboo like carbon nanotube, and multiwalled CNT. Graphene sheet (Fig. S3) consist of multiple layers of graphene where particles in the range of 20–50 nm are dispersed. Moreover, carbon nanotubes with multiple graphene layer (10–15 layers) aligned parallel to the tube axis were also formed during the pyrolysis of melamine as shown in Fig. S3. Interestingly, presence of bamboo-like carbon tubes with multiples compartments in the size of 10 nm, that are divided with 7–9 layers of graphene are also observed. The thickness of the carbon wall was measured to be around 2.6 nm, corresponding to 8–10 layers of non-uniform graphene layer. The disorderness and uniformity on the walls to tubular carbon structure is due to the structural defects arising from the doped nitrogen in the carbon network. The length of the bamboo-CNTs is in the range of hundreds of nanometers to several micrometers with straight and uniform morphology, where NiCo alloyed particles are incorporated in between the compartment with an average size of 10–15 nm in spherical or ellipsoidal shape. A close observation of the bamboo CNT shows two types of morphologies, one with inner diameters that completely bridge, and others with a partial growth of graphene layers between the tube walls as illustrated in Fig. S4. HRTEM in Fig. S5 shows that each nanoparticle is encapsulated with multi-layered graphene sheets. Moreover, the crystal lattice spacing of 0.24 nm represents the (111) crystal plane of NiCo alloy and the surrounded layer with inter layer spacing of 0.32 nm confirms the existence of graphene lattice with (002) crystal plane as observed in XRD profile. The adsorption and decomposition of carbonaceous species on the catalyst surface that reaches to its supersaturation and large amount of carbon atom incorporated to the nanoparticle form a metal-carbide intermediate phase [37]. Based on the previous studies, there should be some evidence of carbide formation in NiCo surface as well. However, any kind of metal carbide phase was not identified in our catalyst using TEM or XPS analysis could be due to the background signal of

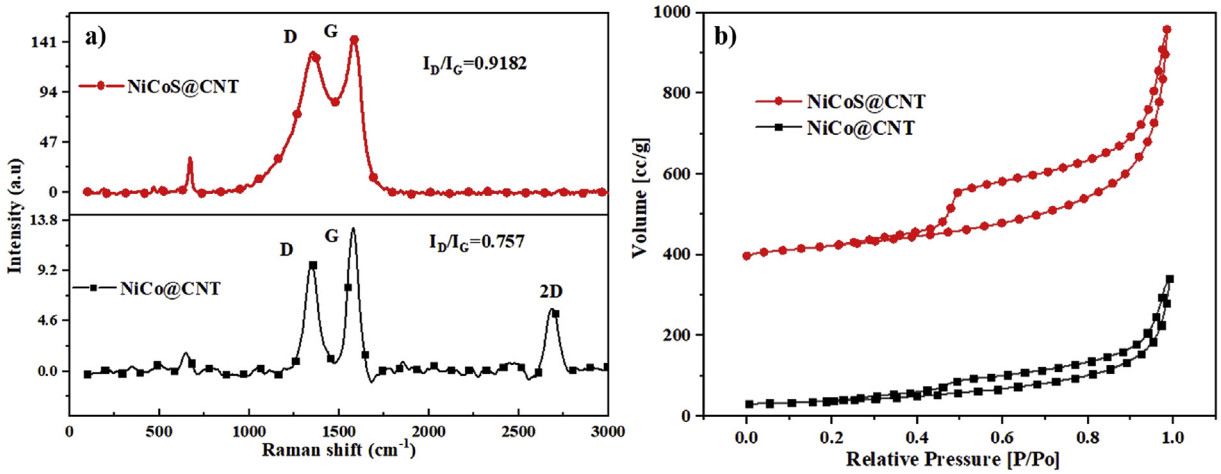

Fig. 2. a) Raman spectrum and corresponding I_D/I_G ratio, b) BET isotherms of synthesized samples. (A colour version of this figure can be viewed online.)

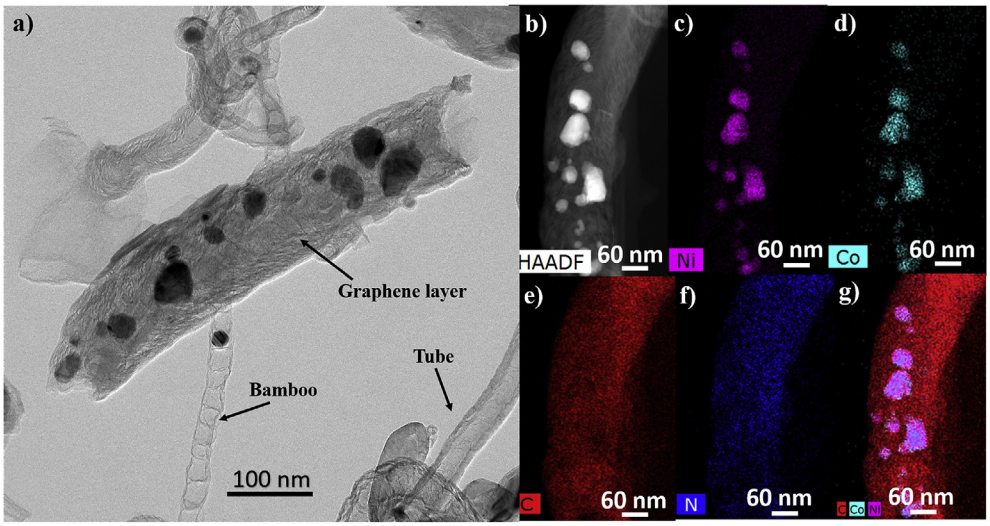

Fig. 3. a) TEM image b) HAADF-STEM image c-d) elemental composition of as-synthesized NiCo@CNT. (A colour version of this figure can be viewed online.)

carbon structure beneath the particle [38].

HAADF-STEM image in Fig. 3b and the corresponding elemental mapping in Fig. 3c–g validates the presence of Ni, Co, C and N on the surface of the catalyst. The elemental phase mapping of Ni and Co where the color composition is uniform everywhere reaffirms the bimetallic NiCo and consistent with XRD and SEM-EDX analysis. Moreover, the presence of N_2 during pyrolysis confirms the successful formation of N doped graphene network that enhances the formation of highly mesoporous to provide highly active sites in the graphene lattice. The metal salt used as a precursor for synthesis not only act as a source of metal nanoparticle encapsulated on the CNT network, but also impart the site for the development of N doped carbon nanotube framework. Xiaoping et al. conducted an experiment without Co^{2+} and the obtained particle contain only carbon nitride sheets, and no sign of CNT formation. This indicates that metal nanoparticle is essential for the exfoliation of carbon nitride formed into well-defined CNTs [39]. Nonetheless, the type of carbon nanotube formed vary based on the metal encapsulated, particle morphology (size, shape, oxidation state and crystal structure), reaction parameters, reaction environment and carbon source.

To provide further insight into the transition of melamine to CNTs, herein we propose a growth mechanism based on the detailed TEM analysis and previous reports. Based on the ordering of graphene layers and the position of graphene layer with respect to the tubular axis, carbon nanotubes can be categorized as four, namely, cup-stacked carbon nano fibers (CNF), single walled carbon nanotubes (SWCNTs), multi walled carbon nanotubes (MWCNTs) and bamboo-like carbon nanotubes (BCNTs) [40–44]. Schematics of the formation of bamboo like structure in NiCo@CNT is shown in Fig. 4. During the in-situ polymerization of melamine, the phase transformation starts at 350 °C and during that period the precursor is in crystalline melamine. The solid-state reaction of melamine with a rise in temperature facilitates the formation of melem ($C_6N_7(NH_2)_3$), where the tris-triazine rings are ended with -NH_2 group, that are the base material for carbon nitride. Melem was further transformed into melon, a repeated tris-triazine ring upon the elimination of ammonium molecule [45]. When the temperature rises to 400 °C, it gets been transformed into a crystallite or an amorphous graphite like carbon nitride with release of protons, and the further increase in the temperature to 500 °C converts thejdhse metastable compounds to g-C_3N_4. Thus formed g-C_3N_4 act as a source of carbon for the formation of CNT and also a source of dopant nitrogen. Meanwhile, the nitrates of nickel and cobalt are decomposed into their amorphous metallic forms and get converted into metal alloy above 600 °C. The presence of metal nanoparticle (NiCo) catalyzes the dissolution of amorphous carbon from C-N bond of C_3N_4 and triggers the formation of graphene layer. The continuous increase in the surface temperature further converts the graphene into different form of CNTs. This observation suggest that the crystallization or graphitization of CNTs was mediated by NiCo metal phase, and the formation of NiCo@CNT process can be termed as “metal-mediated graphitization”. Lin et al. studied the growth dynamic of bamboo-like CNT through the catalytic decomposition of C_2H_2 over Ni catalyst and developed a gas-solid based reaction mechanism for the formation of CNT [46]. The growth of CNT results from the diffusion of carbon atoms and followed by nucleation and growth. The as-mentioned diffusion can be of two ways, i.e., surface diffusion or bulk diffusion to the boundary of metal-graphene interface layer, that further causes the formation of outer graphene layer. During the formation of bamboo like CNT, the stacked inner layer graphene is formed through the diffusion of C atom into the interface of NiCo/Graphene layer. The dominating route for the formation of graphene layer parallel to the tube axis is through the nucleation of C atoms on the base of the symmetric NiCo nanocatalysts. The elongation of the bamboo is through the surface diffusion of C atoms at the NiCo-graphite edge. The continuous accumulation of C atoms at the base of NiCo-graphene interface causes asymmetric change in the particle and more atoms are nucleated on the edge and bottom of the deformed particle, with the formation of bamboo knots over the outer layer as in Fig. 4i. The base diameter of the NiCo particle shrinks with the elongation of the particle with an effective expansion in the interface and surface area of the catalyst (Fig. S6). The asymmetric elongation of the catalyst develops a strain energy on the particle surface. The graphene layers fully encapsulates the lower part of the catalyst and seals the CNT walls internally by making a compartment. A restoring cohesive force developed through an increase in surface tensional force and as well as the compressive stress from the growth walls of the CNTs, provokes the catalytic particle to be released from the newly formed graphene layer and the growth process is repeated to form a complete bamboo like structure with multiple knots (Fig. 4 iii). Based on the knot formation of bamboo CNT, it can be of two types: a) complete knot

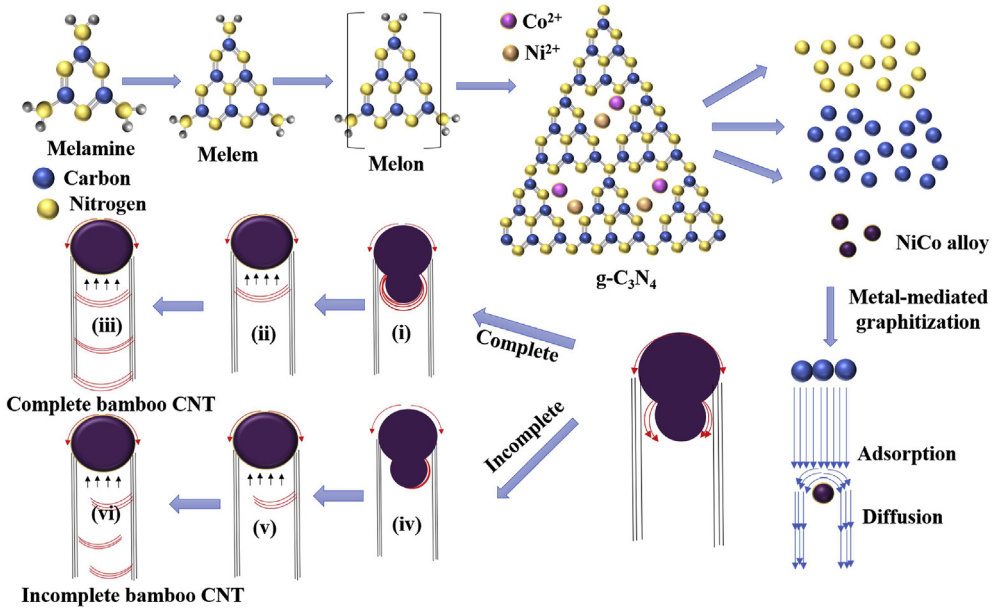

Fig. 4. Schematic representation showing the polymerization of melamine into bamboo like CNT in presence of NiCo nanoparticle. (A colour version of this figure can be viewed online.)

formation and b) incomplete knot formation. A full formation of inner graphene layers and a successful division of each compartment results a complete knot formation. In case of incomplete knot formation, the inner graphene layers are not completely bridged with leaks in between each compartment. Our anticipatory mechanism shows a clear reason for the formation of complete bamboo knot as the full formation of graphene layer before the migration of the catalyst nanoparticle owing to the restoring cohesive forces, and on other hand, the release of particle before the complete graphene layer ends with an incomplete knot formation (Fig. 4iv-vi). The growth mechanism of CNT is specifically different from bamboo CNT and can be described through a chain of adsorption-decomposition-diffusion-nucleation, as highly favorable route. The nucleated carbon atoms that are excreted through the surface of the catalyst and form multiple graphene layer that are in line with the diameter of the catalytic nanoparticle, form MWCNTs.

The growth mechanism of CNT in NiCoS@CNT is same as discussed above, with only difference being the formation of a different alloyed particle. TEM of NiCoS@CNT (Fig. S7) shows the formation of bamboo like CNTs encapsulated with hybrid nanoparticles in the range of 5–20 nm. Interestingly, no clear formation of MWCNTs are visible. The particles are incorporated either on bamboo like CNT or into carbon tubes with no clear graphene walls parallel to the axis. The HAADF-STEM in Fig. 5 shows the presence of particle with different contrast attributed to the presence of hybrid $NiCo/Co_3Ni_6S_8/Co_3O_4$ on NiCoS@CNT. The phase mapping of sulfur (S) shows the successful doping not limited on the surface of the metal catalyst and present on the carbon layer as well. The non-uniform overlapping of multiple colors in Fig. 5h affirms the presence of hybrid particles encapsulated in different carbon structure.

X-ray photoelectron spectroscopy (XPS) analysis was used as a surface sensitive technique to understand the elemental composition and oxidation state of the synthesized material. Surface elemental composition from XPS analysis is given in Table S1. Ni 2p spectrum in Fig. 6a consist of two spin orbital doublet centered at 855.3 ± 0.4 eV and 873.3 ± 0.3 eV corresponding to Ni $2p_{3/2}$ and Ni $2p_{1/2}$ orbitals respectively, along with two other weak satellite peaks at 861.9 ± 0.2 eV and 880.8 ± 0.4 eV [47–49]. The deconvolution of each peak shows the existence of two sub-peaks attributed to the existence of Ni^{2+} and Ni^{3+} valence state of Ni. In the Co 2p XPS spectrum shown in Fig. 6b, there appears two intense peak due to the spin orbital splitting of Co $2p_{3/2}$ and Co $2p_{1/2}$ with 15.8 eV energy separation [50,51]. The fitted Co 2p spectrum confirms the existence of Co in +3 and + 2 oxidation state. Moreover, there appears an intense satellite peak around 6 eV greater than the main peak that can be ascribed to the spin orbital of Co^{2+}. A difference in the ratio of Co^{2+}/Co^{3+} for NiCoS@CNT and NiCo@CNT were observed, with calculated values being 0.52 and 0.38 respectively. A higher ratio of Co^{2+}/Co^{3+} is reported to be an indication of higher oxygen vacancies [52,53]. These results confirm the co-existence of Co and Ni in their mixed oxidation state of Ni^{2+}, Ni^{3+}, Co^{2+} and Co^{3+}. However, a close observation of each peak suggests a shifting towards higher binding energy for NiCoS@CNT compared to NiCo@CNT as indicated by dotted lines in Fig. 6a and b. These pronounced peak shifts could be due to a strong migration of electron cloud induced by the doping of a higher electronegative S atom into the metallic lattice that particularly improves the electron coupling.

The core level XPS spectrum of O 1s in NiCo@CNT and NiCoS@CNT are shown in Fig. 6c and d, which can be classified into three oxidation states of oxygen. O_L peak observed at 529.8 eV corresponds to O_2^- oxidation state that are bonded to the metal lattice on the surface. O_V peak centered at 531.4 eV are related to the non-stoichiometric oxygen that originate from the oxygen vacancies on the surface, which are specifically significant for electrochemical applications. The peak O_C around 532.8 eV refers to the presence of hydroxyl group or moisture oxygen adsorbed on the particle surface from the surrounding environment (O_2, $-CO_3$ and -OH) [54,55]. Both the sample have these three peaks in the variation of ±0.2 eV. The relative area of O_v/O_T, where O_T is the sum of areas of O_L, O_V and O_C, can be used to measure the level of oxygen vacancy defects on the surface lattice through the distortion of the crystal structure. The ratio of Ov/O_T improved from 0.67 to 0.79 for NiCo@ CNT and NiCoS@CNT respectively. The calculated results reveals that the presence of sulfur during doping improves the amount of oxygen vacancies on the surface, which could enhance

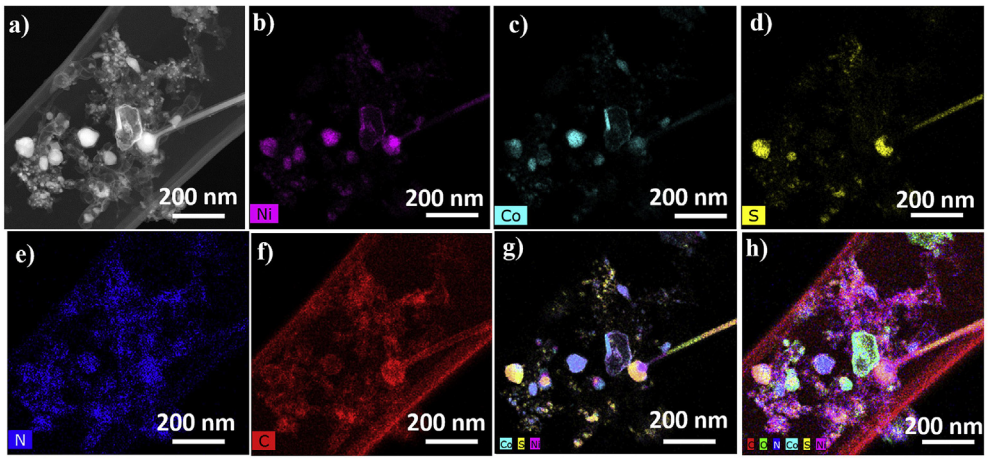

Fig. 5. a) HAADF STEM mapping and b-h) EDX mapping result of NiCoS@CNT. (A colour version of this figure can be viewed online.)

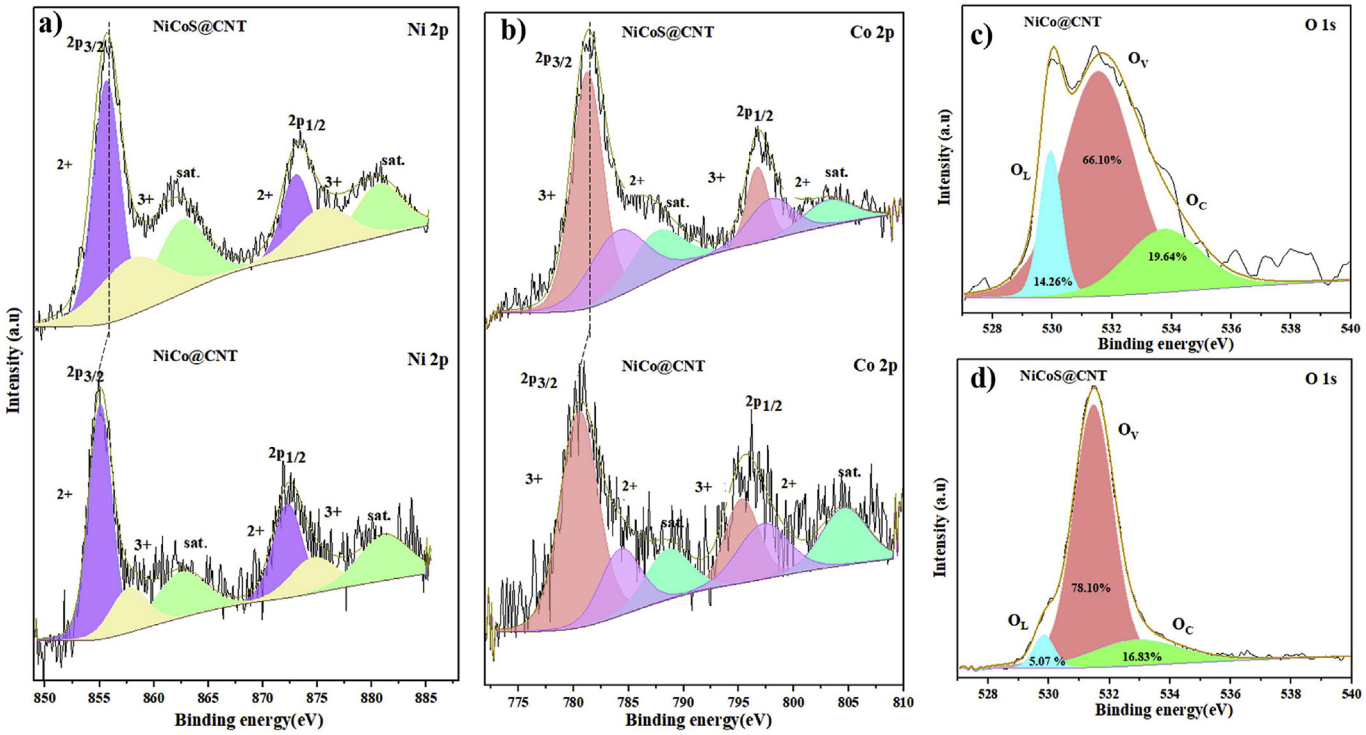

Fig. 6. XPS deconvolution spectrum of a) Ni 2p b)Co 2p and c-d)O 1s of NiCo@CNT and NiCoS@CNT. (A colour version of this figure can be viewed online.)

the ability to adsorb the reactants/intermediates during electrochemical reactions.

XPS C1s profile of NiCo@CNT and NiCoS@CNT with different bonding configuration of C atom are shown in Fig. S8. In NiCo@CNT, the main peak at 284.9 eV corresponds to the presence of sp^2 hybridized C-C bond on the graphitic honeycomb structured lattice [56,57]. The carbon atoms that are bonded with N atoms on the surface of the graphitic lattice could appear at higher binding energy owing to the bonding of lower electronegative C atom (2.55) to higher electronegative N atoms (3.04) [58]. The secondary peak at 285.6 eV can be designated to the sp^2 hybridized C atom bonded to the N atom on graphene lattice, which corresponds to either pyridinic N or graphitic N bond. The ternary peak centered at 286.8 eV corresponds to sp^2 hybridized carbon atoms bonded to the N atoms in Pyrrolic N bonded lattice network. The broad weak peak around 290.56 eV can be ascribed to the formation of C-O bond from the physiosorbed oxygen on the graphene lattice.

XPS deconvolution of N 1s spectrum in Fig. S9 consists of three characteristics peaks corresponding to Pyridinic N, Pyrrolic N and Pyridinic *N*-O centered at 399.1 eV (399.1 eV), 401.56 eV (401.26 eV) and 403.2 eV (403.3 eV) respectively for NiCo@CNT (NiCoS@CNT). These results suggest that N atoms are covalently bonded to the graphene network. Fig. S9a shows the schematic diagram of graphene lattice bonded with N atoms in four different ways. Pyridinic N bonding originates from the π bonding of sp^2 hybridized N atoms with two neighboring sp^2 hybridized C atoms that contributes one p-electron at the edges (or defects) of graphene network [59–61]. Pyrrolic N bonding corresponds to N atoms that integrate in a five membered heterocyclic ring using a π bond with two p-electrons. The characteristic peak at high binding energy (~403.2 eV) can be

attributed to pyridinic N oxide [62]. Out of these bonding, the six-membered cyclic ring structure of pristine graphene lattice was interrupted by Pyrrolic N bonding and forms a sp^3 hybridization and defect doping [63]. XPS deconvolution spectrum shows that Pyrrolic N bonding for NiCoS@CNT (33.85%) is higher than NiCo@CNT (24.31%). Moreover, nitrogen atom in pyridinic state are more prominent than other oxidation states of nitrogen. Graphitic N bonding formed by the substitution of carbon I atom in a hexagonal ring with sp^2 hybridized N atom and is bonded to the neighboring three sp^3 hybridized carbon atoms that would possibly be present between 400.1 and 403 eV, is not visible here. This indicates that the sample is dominated by Pyridinic N bonding and the presence of graphitic N bonding is very limited. This result confirms that the C 1s peak in Fig. S8 at 285.6 eV could be ascribed to the *N*- sp^3 C bond (pyridinic N) rather than *N*-sp^2 C bond (graphitic N). Notably, the higher Pyridinic N acts as an active anchoring site for in-situ growth of metal nanoparticles. The greater N content (6.92%) and the higher percentage Pyridinic N peak (58.3%) significantly improves the electrochemical properties in NiCoS@CNT [64].

XPS spectrum of S 2p in Fig. S10 can be fitted into five peaks: two major peaks at 162.0 eV and 163.4 eV with a splitting energy of 1.4 eV are respectively assigned to the S $2P_{3/2}$ and S $2P_{1/2}$, resulted from the sulfur atoms doped on the metal surface of $Co_3Ni_6S_8$. The XPS peaks at 164.9 eV, 168.43 eV and 167.7 eV corresponding to C=S, C-SO^2-C and C-SO^3-C respectively, confirm that S atoms are successfully incorporated into the C atoms in the graphene lattice.

3.2. Electrochemical analysis

Fig. 7a show the LSV polarization profile of NiCo@CNT, NiCoS@CNT and commercial Pt/C (20%) in an electrolyte of 1 M KOH. When compared with commercial Pt/C, the NiCo@CNT which needed 330 mV overpotential to produce 10 $mAcm^{-2}$ current density, where NiCoS@CNT shows significantly better enhancement in HER performance and needed only 198 mV to achieve the same current density. The obtained Tafel slope of 148 $mVdec^{-1}$ and 87 $mVdec^{-1}$ for NiCo@CNT and NiCoS@CNT respectively exhibited higher HER kinetics for sulfur doped NiCo particles. The durability and stability of NiCoS@CNT towards HER was calculated through multiple cyclic voltammetry run and long-term electrolysis at constant potential. The long-term current-time profile at a constant potential of 0.26 V shows that the current density was maintained at around 10 $mAcm^{-2}$ without any noticeable degradation for 38 h. The inset Fig. 7c(i) of working electrode signifies that the catalyst is very active for HER with higher number of H_2 bubbles produced on the surface of the electrode. Moreover, NiCoS@CNT in inset Fig. 7c(ii) shows no obvious degradation on the LSV when compared to the initial LSV profile, even after a continuous 1000 cycle run between +0.2 and −0.4 V vs RHE at 50 mVs^{-1} scan rates. The superior activity of NiCoS@CNT compared to NiCo@CNT was further demonstrated by EIS analysis as in Fig. 7d. The two semicircular loops in the Nyquist plot confirm that no mass transport limitations exist on the measured potential for both the catalyst. The shorter diameter of the Nyquist plot for NiCoS@CNT corresponds to a decrease in the barrier for the HER performance than NiCo@CNT. Intriguingly, these results confirm that NiCoS@CNT works as an excellent catalyst for HER without compromising the stability and durability. The superior HER activity of NiCoS@CNT could be attributed to the synergetic effect between the macroscopic morphological characteristics and microscopic atomic scale features.

The electrocatalytic performance of the as-prepared catalysts for OER was further studied in an electrolyte of 1 M KOH. OER polarization curve in Fig. 8a presents an intense peak around 1.26 V in NiCoS@CNT corresponding to the oxidation of Ni(II)/Ni(III) or Co(II)/Co(III) which have been studied in detail in many Ni or Co based catalyst [65,66]. The magnified OER plot between 1.2 and 1.45 V in Fig. S11 shows a narrow increase in the current density for NiCo@CNT as well, but much lower than the NiCoS@CNT. This result signifies the presence of more Co^{3+} content in NiCoS@CNT (XRD in Fig. 1a), acting as an electrophilic agent that effectively facilitates the formation of CoOOH and also enhances the adsorption of OH^- ions from the alkaline solution. Thus the formation of Co^{3+} is more likely the reason for the higher OER activity. The current density of NiCoS@CNT is higher than NiCo@CNT at any applied potential, and NiCoS@CNT (295 mV) requires much lower overpotential to reach 10 $mAcm^{-2}$ current density than NiCo@CNT (350 mV), which suggests than sulfur based NiCo catalyst shows higher intrinsic electrochemical OER property than the un-doped catalyst. Moreover, the kinetic parameters of OER were further deducted from the Tafel plot in Fig. 8b, where, NiCoS@CNT shows considerably lower Tafel slope of 78 $mVdec^{-1}$ than NiCo@CNT holding a value of 92 $mVdec^{-1}$ demonstrating a faster charge transfer reaction in NiCoS@CNT.

To understand the various resistance related to the charge transfer process and the enhancement in the electron transport during electrochemical OER one can refer to the EIS analysis in Fig. 8c. Importantly, the semicircular loop diameter of NiCoS@CNT is much smaller than NiCo@CNT at 1.55 V underlining the lower contact impedance and faster charge transfer of hybrid sulfur doper NiCo material anchored over the carbon tubes. A simple Randle circuit model (inset Fig. 8c) comprising of a series resistance (R_s), constant phase element (CPE) and charge transfer resistance (R_{ct}) can be used to fit the obtained Nyquist plot. The series resistance R_s corresponds to the overall electrolyte resistance that includes the contact resistance and the bulk material resistance that can be measured from the intercept of the Nyquist plot with y-axis at higher frequency. The charge transfer resistance R_{ct}, at the catalyst-solution interface can be identified from the diameter of the Nyquist plot at a region of higher frequency. The constant phase element (CPE) is a replacement of double layer capacitive effect of the OER in the entire system that provides insights of the structural reconstruction and the oxide layer conductivity. The series resistance (R_s) fitted from EIS Nyquist profile gives a resistance value of 12.3 Ω and 7.5 Ω respectively for NiCo@CNT and NiCoS@CNT, whereas the fitted R_{ct} values following a similar trend (R_{ct}-NiCo@CNT = 42Ω and R_{ct}-NiCoS@CNT = 29Ω) undoubtedly confirm the faster charge transfer in NiCoS@CNT greatly influences the superior activity and reaction kinetics of OER as indicated in Tafel plot. Moreover, the double layer capacitive value (C_{dl}) of NiCoS/CNT (calculated to be 6.23 $mFcm^{-2}$) and NiCo/CNT (4.6 $mFcm^{-2}$) suggest that NiCoS/CNT possesses more active sites exposed to the electrolyte that facilitate a faster charge transfer reaction between the catalyst-electrolyte interface for the electrochemical reactions. The inset Figure shows that the EIS profile of NiCoS@CNT at different potential exhibits a decrease in the diameter of the semicircular loop with an increase in the applied potential, indicating a reduction in the barrier of the interfacial OER mechanism. The fitted values of R_s, R_{ct} and C_{dl} at different potentials are represented in Table S1. R_s, shows an unexpected increase in the resistance value, which could be due to the presence of oxygen bubbles on the electrode surface that resist the passage of OH^- adsorption and electron transfer [67].

The durability of the NiCoS@CNT was measured using the multiple CV run for 2000 cycles, presented in Fig. 8d, shows negligible loss in the current density. The absence of oxidation peak after the stability run at 1.26 V could be due to some surface modifications of the catalyst as reported elsewhere [67–69]. As the peak is possibly associated with Co^{2+}/Co^{3+} (based on XRD, Fig. 1a),

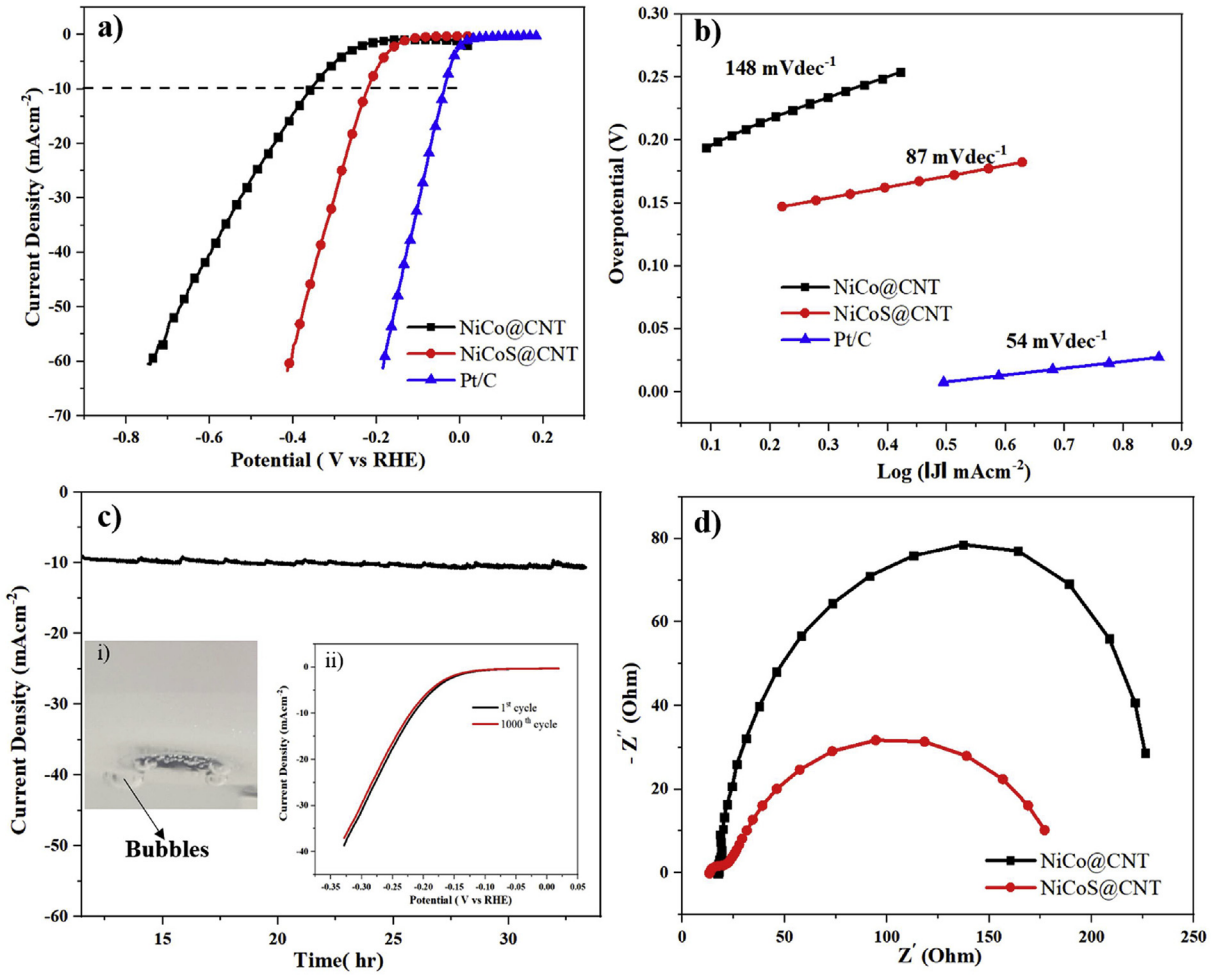

Fig. 7. a) LSV polarization curve and b) Tafel plot of NiCo@CNT, NiCoS@CNT and commercial Pt/C (20%) for HER in a KOH solution of 1 M at 5 mVs^{-1} scan rate c) time dependent current density curve of NiCoS@CNT under constant potential of 0.26 V for 38 h. The inset (i) shows the glassy carbon working electrode loaded with NiCoS@CNT for the HER operation at 0.4 V with H_2 bubbles generated at electrode surface (ii) polarization curve recorded for NiCoS@CNT before and after 1000 cycle of CV stability run d) EIS spectrum at −0.3 V for NiCo@CNT and NiCoS@CNT. (A colour version of this figure can be viewed online.)

a possible change in Co_3O_4 phase is anticipated after the stability test; nonetheless the catalytic activity is not significantly compromised, which indicates the other phases to be responsible for high activity as compared to the Co_3O_4. Also a slight improvement in current density can be seen after the multiple cycle, which could be due to the restructuring of the catalyst surface to a more active and stable phase after several continuous oxidation and reduction cycle. Collectively, these results suggest the excellent OER performance of NiCoS@CNT with superior activity and durability. According to previous reports, Co^{3+} is the active site of OER, and DFT analysis shows that the two electrons close to the oxygen vacancy that are related to oxygen 2p orbital will enable the nearby Co^{3+} atoms by delocalization and thereby activate the low-coordinated Co^{3+} ions for an effective adsorption of H_2O. Moreover, the excitation of the delocalized electrons near to oxygen vacancy enhances the conductivity and electrochemical properties of the catalyst. The strong oxidation peak in the LSV of NiCoS@CNT (Fig. 8a), not observed in NiCo@CNT, facilitates the oxidation of Co^{3+} to Co^{4+} over highly conductive carbon network to enhance the OER process. The surface dominated adsorption and formation of OH^-, O^{2-} and OOH^- intermediates are mediated by utilizing the Co^{3+} ions embedded in the conductive carbon framework. The oxidation of Co^{3+} to Co^{4+} improves the electrophilicity of the catalyst surface and promotes the adsorption of nucleophilic species such as OH^- for the conversion to OOH^- intermediates [54]. Additionally; the high surface area and porosity, greater degree of lattice surface defect, more Pyridine N content, and high oxygen vacancies improved the electronic conductivity of carbon nanotubes. The abundance of active sites and wettability also contribute towards the outstanding OER performance in NiCoS@CNT.

Next, a two-electrode configuration was developed, using the highly active and stable catalysts for HER and OER as cathode and anode respectively to perform water splitting reaction in nitrogen-saturated 1 M KOH electrolyte as displayed in the schematic of Fig. 9a inset. Interestingly, NiCoS@CNT reaches the 10 $mAcm^{-2}$ current density at 1.53 V cell voltage, that is 120 mV lower than for NiCo@CNT. The inset image in Fig. 9b confirms the overall water splitting performance of NiCoS@CNT with large amount of H_2 and O_2 gas evolved during the HER and OER performance respectively. The chronoamperometric test of NiCoS@CNT at a fixed potential of 1.53 V for 24 h displays an excellent stable performance with a constant current density of 10 $mAcm^{-2}$ for the entire evaluation period. The remarkable electrocatalytic performance including high activity and stability of hybrid NiCoS@CNT makes it a potential replacement for HER and OER commercial catalyst.

The current state-of-the-art of some selected Ni-Co based catalyst for OER, HER and water splitting processes are detailed in Table S3. The superior electrocatalytic performance of NiCoS@CNT

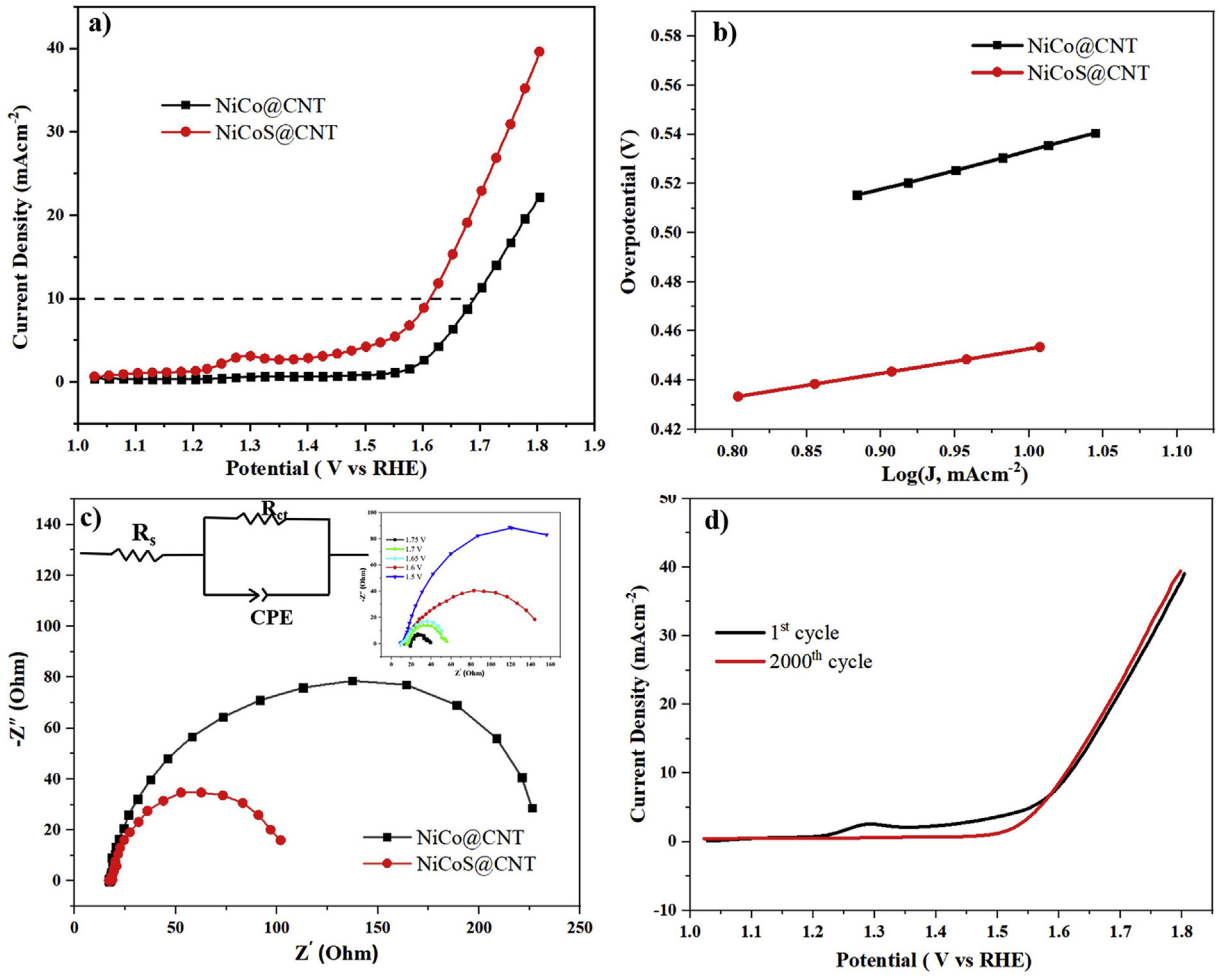

Fig. 8. a) OER polarization curve, b) Tafel plot of NiCo@CNT and NiCoS@CNT in 1 M KOH, c) EIS measurement at 1.55 V on NiCo@CNT and NiCoS@CNT. Inset shows the impedance spectrum of NiCoS@CNT at different potential and the equivalent circuit diagram consist of a series resistance (R_s), a charge transfer resistance (R_{ct}) and constant phase element (CPE) d) LSV curve of NiCoS@CNT before and after 2000 cycle of CV stability run. (A colour version of this figure can be viewed online.)

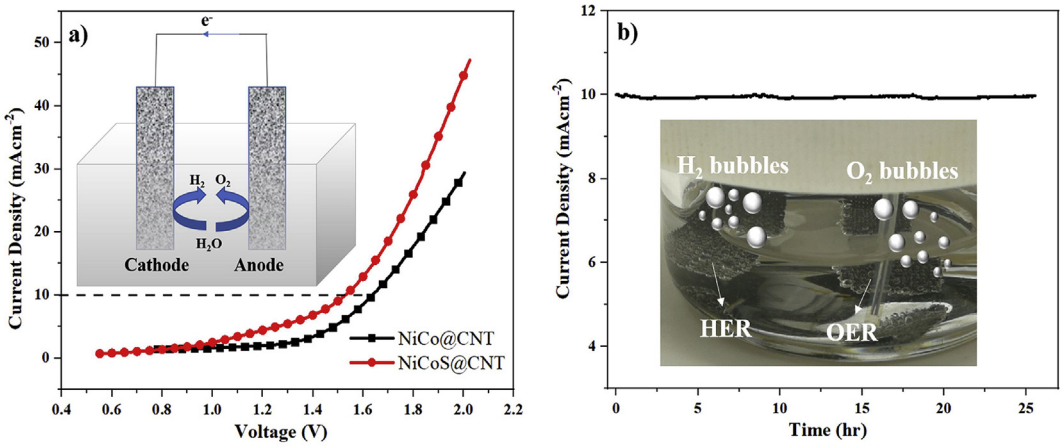

Fig. 9. a) LSV plot of water electrolysis of NiCo@CNT and NiCoS@CNT in a two-electrode configuration with 2 mVs^{-1} scan rate. Inset schematic diagram of an electrolyzer b) Chronoamperometric (CA) analysis of NiCoS@CNT at 1.53 V in an electrolyte of 1 M KOH. Inset image displays the presence of gas bubbles corresponding to the H_2 and O_2 production. (A colour version of this figure can be viewed online.)

on overall water splitting is ascribed to the synergetic effects of the particles incorporated with the CNT framework and the unique macroscopic structural characteristics. The synthesized particles show exceptionally high active surface area to facilitate the adsorption of reactive species and their subsequent electrochemical reaction. Well defined mesoporous morphology allows a better penetration of electrolyte and thereby efficient utilization of active sites. The N and S dopant on the surface also contribute to the

electrocatalytic performance to a great extent. The abundant oxygen vacancies play a key role in promoting the surface interactions. While taking the benefit of a unique hierarchical architecture, the electrochemical performance of both HER and OER are significantly improved. Looking at the low concentrations of Ni and Co (<0.5% for NiCo@CNT and <1.5% for NiCoS@CNT), the formation of single atoms doped CNT and their contribution towards electrocatalytic performance enhancement could be significant. A detained study on the synthesis and optimization of single atoms density is planned for future to understand the catalytic properties of single atom doped CNT acting as active sites as compared to the nanoparticles present on CNT.

4. Conclusion

To summarize, a hybrid S-doped NiCo particle incorporated in N doped carbon nanotubes with high surface area and enriched oxygen vacancies are successfully synthesized using an economical way of pyrolysis of melamine as a source of carbon. The same experimental procedure was followed without adding a sulfur source with the alloyed NiCo nanoparticles embedded on carbon nanotube. The presence of sulfur thereby changed not only the morphological characteristics, but also tuned the electrochemical properties. The as-synthesized hybrid material demonstrated excellent activity and durability towards both HER and OER. The NiCoS@CNT as a cathode catalyst, shows significantly better enhancement in HER performance with an overpotential of 198 mV to reach 10 $mAcm^{-2}$ and a small Tafel slope of 87 $mVdec^{-1}$. The NiCoS@CNT as an anode catalyst displayed an excellent OER activity with an overpotential of 295 mV to reach 10 $mAcm^{-2}$ with a small Tafel slope of 78 $mVdec^{-1}$. While considering NiCoS@CNT as both anode and cathode catalysts in an overall water splitting reaction, the catalyst only required 1.53 V cell voltage to deliver a current density of 10 $mAcm^{-2}$ and exhibited a long-term stability in bulk water electrolysis under alkaline conditions. Based on the results, we believe that this facile, simple and cost-effective pyrolysis of melamine-metal salt synthesis strategy could be useful for the development of highly efficient electrocatalyst in many electrochemical reactions with a potential for large-scale industrial applications.

CRediT authorship contribution statement

Anchu Ashok: Conceptualization, Methodology, Data curation, Formal analysis, Investigation, Validation, Writing - original draft. **Anand Kumar:** Conceptualization, Supervision, Writing - review & editing, Project administration, Funding acquisition. **Janarthanan Ponraj:** Visualization, Investigation. **Said A. Mansour:** Visualization, Investigation.

Declaration of competing interest

The authors declare that they have no known competing financial interests or personal relationships that could have appeared to influence the work reported in this paper.

Acknowledgement

This publication was made possible by NPRP grant (NPRP8–145–2–066) from the Qatar National Research Fund (a member of Qatar Foundation). The statements made herein are solely the responsibility of the author(s). The authors also wish to gratefully acknowledge Centre of Advanced Materials (CAM) for XRD analysis and the SEM analysis was accomplished in the Central Laboratories Unit, Qatar University. The authors would also like to acknowledge QEERI Core Labs for their support related to the TEM characterization. Open Access funding provided by the Qatar National Library (QNL).

Appendix A. Supplementary data

Supplementary data to this article can be found online at https://doi.org/10.1016/j.carbon.2020.08.047.

References

[1] Z. Wang, D. Xu, J. Xu, X. Zhang, Oxygen electrocatalysts in metal–air batteries: from aqueous to nonaqueous electrolytes, Chem. Soc. Rev. 43 (2014) 7746–7786.
[2] L. Dai, Y. Xue, L. Qu, H. Choi, J. Baek, Metal-free catalysts for oxygen reduction reaction, Chem. Rev. 115 (2015) 4823–4892.
[3] Y. Jiao, Y. Zheng, M. Jaroniec, S.Z. Qiao, Design of electrocatalysts for oxygen- and hydrogen-involving energy conversion reactions, Chem. Soc. Rev. 44 (2015) 2060–2086.
[4] M.S. Faber, S. Jin, Earth-abundant inorganic electrocatalysts and their nanostructures for energy conversion applications, Energy Environ. Sci. 7 (2014) 3519–3542.
[5] M. Dresselhaus, I. Thomas, Alternative energy technologies, Nature 414 (2001) 332.
[6] J.A. Turner, Sustainable hydrogen production, Science 305 (2004) 972–974.
[7] T. Wang, L. Wu, X. Xu, Y. Sun, Y. Wang, W. Zhong, Y. Du, An efficient Co_3S_4/CoP hybrid catalyst for electrocatalytic hydrogen evolution, Sci. Rep. 7 (2017) 11891.
[8] X. Zou, X. Huang, A. Goswami, R. Silva, B.R. Sathe, E. Mikmeková, T. Asefa, Cobalt-embedded nitrogen-rich carbon nanotubes efficiently catalyze hydrogen evolution reaction at all pH values, Angew. Chem. Int. Ed. 53 (2014) 4372–4376.
[9] J. Li, M. Yan, X. Zhou, Z. Huang, Z. Xia, C. Chang, Y. Ma, Y. Qu, Mechanistic insights on ternary $Ni_{2-x}Co_xP$ for hydrogen evolution and their hybrids with graphene as highly efficient and robust catalysts for overall water splitting, Adv. Funct. Mater. 26 (2016) 6785–6796.
[10] P. Chen, T. Zhou, M. Zhang, Y. Tong, C. Zhong, N. Zhang, L. Zhang, C. Wu, Y. Xie, 3D nitrogen-anion-decorated nickel sulfides for highly efficient overall water splitting, Adv. Mater. 29 (2017) 1701584.
[11] Y. Hou, Z. Wen, S. Cui, S. Ci, S. Mao, J. Chen, An advanced nitrogen-doped graphene/cobalt-embedded porous carbon polyhedron hybrid for efficient catalysis of oxygen reduction and water splitting, Adv. Funct. Mater. 25 (2015) 872–882.
[12] A. Ashok, A. Kumar, M.A. Matin, F. Tarlochan, Synthesis of highly efficient bifunctional Ag/Co_3O_4 catalyst for oxygen reduction and oxygen evolution reactions in alkaline medium, ACS Omega 3 (2018) 7745–7756.
[13] A. Ashok, A. Kumar, J. Ponraj, S.A. Mansour, F. Tarlochan, Single step synthesis of porous $NiCoO_2$ for effective electrooxidation of glycerol in alkaline medium, J. Electrochem. Soc. 165 (2018) J3301–J3309.
[14] T. Kwon, H. Hwang, Y.J. Sa, J. Park, H. Baik, S.H. Joo, K. Lee, Cobalt assisted synthesis of IrCu hollow octahedral nanocages as highly active electrocatalysts toward oxygen evolution reaction, Adv. Funct. Mater. 27 (2017) 1604688.
[15] E. Fabbri, A. Habereder, K. Waltar, R. Kötz, T.J. Schmidt, Developments and perspectives of oxide-based catalysts for the oxygen evolution reaction, Catal. Sci. Technol. 4 (2014) 3800–3821.
[16] T. Audichon, E. Mayousse, S. Morisset, C. Morais, C. Comminges, T.W. Napporn, K.B. Kokoh, Electroactivity of RuO_2–IrO_2 mixed nanocatalysts toward the oxygen evolution reaction in a water electrolyzer supplied by a solar profile, Int. J. Hydrogen Energy 39 (2014) 16785–16796.
[17] H. Du, Y. Li, F. Ding, J. Zhao, X. Zhang, Y. Li, R. Zhao, M. Cao, T. Yu, X. Xu, Boosting the capacitance of $NiCo_2O_4$ hierarchical structures on nickel foam in supercapacitors, Int. J. Hydrogen Energy 43 (2018) 15348–15357.
[18] J. Hu, L. Shi, Q. Liu, H. Huang, T. Jiao, Improved oxygen reduction activity on silver-modified $LaMnO_3$–graphene via shortens the conduction path of adsorbed oxygen, RSC Adv. 5 (2015) 92096–92106.
[19] F. Song, K. Schenk, X. Hu, A nanoporous oxygen evolution catalyst synthesized by selective electrochemical etching of perovskite hydroxide $CoSn(OH)_6$ nanocubes,, Energy Environ. Sci. 9 (2016) 473–477.
[20] Y. Wang, C. He, A. Brouzgou, Y. Liang, R. Fu, D. Wu, P. Tsiakaras, S. Song, A facile soft-template synthesis of ordered mesoporous carbon/tungsten carbide composites with high surface area for methanol electrooxidation,, J. Power Sources 200 (2012) 8–13.
[21] X. Zhang, P.K. Shen, Glycerol electrooxidation on highly active Pd supported carbide/C aerogel composites catalysts, Int. J. Hydrogen Energy 38 (2013) 2257–2262.
[22] Y. Tang, C. Liu, W. Huang, X. Wang, L. Dong, S. Li, Y. Lan, Bimetallic carbides-based nanocomposite as superior electrocatalyst for oxygen evolution reaction, ACS Appl. Mater. Interfaces 9 (2017) 16977–16985.
[23] D. Kong, J.J. Cha, H. Wang, H.R. Lee, Y. Cui, First-row transition metal dichalcogenide catalysts for hydrogen evolution reaction, Energy Environ. Sci. 6

(2013) 3553–3558.
[24] X. Gao, H. Zhang, Q. Li, X. Yu, Z. Hong, X. Zhang, C. Liang, Z. Lin, Hierarchical $NiCo_2O_4$ hollow microcuboids as bifunctional electrocatalysts for overall water-splitting, Angew. Chem. Int. Ed. 55 (2016) 6290–6294.
[25] C. Huang, T. Ouyang, Y. Zou, N. Li, Z. Liu, Ultrathin $NiCo_2P_x$ nanosheets strongly coupled with CNTs as efficient and robust electrocatalysts for overall water splitting, J. Mater. Chem. 6 (2018) 7420–7427.
[26] J. Li, M. Yan, X. Zhou, Z. Huang, Z. Xia, C. Chang, Y. Ma, Y. Qu, Mechanistic insights on ternary $Ni_{2-x}Co_xP$ for hydrogen evolution and their hybrids with graphene as highly efficient and robust catalysts for overall water splitting, Adv. Funct. Mater. 26 (2016) 6785–6796.
[27] W. Zhu, X. Yue, W. Zhang, S. Yu, Y. Zhang, J. Wang, J. Wang, Nickel sulfide microsphere film on Ni foam as an efficient bifunctional electrocatalyst for overall water splitting, Chem. Commun. 52 (2016) 1486–1489.
[28] W. Zhu, Z. Yue, W. Zhang, N. Hu, Z. Luo, M. Ren, Z. Xu, Z. Wei, Y. Suo, J. Wang, Wet-chemistry topotactic synthesis of bimetallic iron–nickel sulfide nanoarrays: an advanced and versatile catalyst for energy efficient overall water and urea electrolysis, J. Mater. Chem. 6 (2018) 4346–4353.
[29] G. Zhang, Y. Feng, W. Lu, D. He, C. Wang, Y. Li, X. Wang, F. Cao, Enhanced catalysis of electrochemical overall water splitting in alkaline media by Fe doping in Ni_3S_2 nanosheet arrays, ACS Catal. 8 (2018) 5431–5441.
[30] H. Wang, Z. Li, G. Li, F. Peng, H. Yu, Co_3S_4/NCNTs: a catalyst for oxygen evolution reaction,, Catal. Today 245 (2015) 74–78.
[31] N. Mahmood, C. Zhang, J. Jiang, F. Liu, Y. Hou, Multifunctional Co_3S_4/graphene composites for lithium ion batteries and oxygen reduction reaction, Chem-A Eur. J. 19 (2013) 5183–5190.
[32] M. Zhu, Z. Zhang, H. Zhang, H. Zhang, X. Zhang, L. Zhang, S. Wang, Hydrophilic cobalt sulfide nanosheets as a bifunctional catalyst for oxygen and hydrogen evolution in electrolysis of alkaline aqueous solution, J. Colloid Interface Sci. 509 (2018) 522–528.
[33] S. Shit, S. Chhetri, W. Jang, N.C. Murmu, H. Koo, P. Samanta, T. Kuila, Cobalt sulfide/nickel sulfide heterostructure directly grown on nickel foam: an efficient and durable electrocatalyst for overall water splitting application, ACS Appl. Mater. Interfaces 10 (2018) 27712–27722.
[34] Z. Liu, K. Xiao, Q. Xu, N. Li, Y. Su, H. Wang, S. Chen, Fabrication of hierarchical flower-like super-structures consisting of porous $NiCo_2O_4$ nanosheets and their electrochemical and magnetic properties, RSC Adv. 3 (2013) 4372–4380.
[35] L. Malard, M. Pimenta, G. Dresselhaus, M. Dresselhaus, Raman spectroscopy in graphene, Phys. Rep. 473 (2009) 51–87.
[36] L.G. Cançado, A. Jorio, E.M. Ferreira, F. Stavale, C.A. Achete, R.B. Capaz, Moutinho, Marcus Vinicius de Oliveira, A. Lombardo, T. Kulmala, A.C. Ferrari, Quantifying defects in graphene via Raman spectroscopy at different excitation energies, Nano Lett. 11 (2011) 3190–3196.
[37] J. Gavillet, A. Loiseau, C. Journet, F. Willaime, F. Ducastelle, J. Charlier, Root-growth mechanism for single-wall carbon nanotubes, Phys. Rev. Lett. 87 (2001) 275504.
[38] D.R. Minett, J.P. O'Byrne, S.I. Pascu, P.K. Plucinski, R.E. Owen, M.D. Jones, D. Mattia, Fe@ CNT-monoliths for the conversion of carbon dioxide to hydrocarbons: structural characterisation and Fischer–Tropsch reactivity investigations, Catal. Sci. Technol. 4 (2014) 3351–3358.
[39] X. Dai, Z. Li, Y. Ma, M. Liu, K. Du, H. Su, H. Zhuo, L. Yu, H. Sun, X. Zhang, Metallic cobalt encapsulated in bamboo-like and nitrogen-rich carbonitride nanotubes for hydrogen evolution reaction, ACS Appl. Mater. Interfaces 8 (2016) 6439–6448.
[40] M. Endo, Y.A. Kim, M. Ezaka, K. Osada, T. Yanagisawa, T. Hayashi, M. Terrones, M.S. Dresselhaus, Selective and efficient impregnation of metal nanoparticles on cup-stacked-type carbon nanofibers, Nano Lett. 3 (2003) 723–726.
[41] M. Endo, Y. Kim, T. Hayashi, Y. Fukai, K. Oshida, M. Terrones, T. Yanagisawa, S. Higaki, M. Dresselhaus, Structural characterization of cup-stacked-type nanofibers with an entirely hollow core, Appl. Phys. Lett. 80 (2002) 1267–1269.
[42] F.H. Gojny, J. Nastalczyk, Z. Roslaniec, K. Schulte, Surface modified multi-walled carbon nanotubes in CNT/epoxy-composites, Chem. Phys. Lett. 370 (2003) 820–824.
[43] M. Castellino, V. Stolojan, A. Virga, M. Rovere, K. Cabiale, M.R. Galloni, A. Tagliaferro, Chemico-physical characterisation and in vivo biocompatibility assessment of DLC-coated coronary stents, Anal. Bioanal. Chem. 405 (2013) 321–329.
[44] C.J. Lee, J. Park, Growth model of bamboo-shaped carbon nanotubes by thermal chemical vapor deposition, Appl. Phys. Lett. 77 (2000) 3397–3399.
[45] C. Hu, Y. Chu, M. Wang, X. Wu, Rapid synthesis of g-C_3N_4 spheres using microwave-assisted solvothermal method for enhanced photocatalytic activity, J. Photochem. Photobiol., A 348 (2017) 8–17.
[46] M. Lin, J.P.Y. Tan, C. Boothroyd, K.P. Loh, E.S. Tok, Y. Foo, Dynamical observation of bamboo-like carbon nanotube growth, Nano Lett. 7 (2007) 2234–2238.
[47] A. Ashok, A. Kumar, J. Ponraj, S.A. Mansour, F. Tarlochan, Effect of Ni incorporation in cobalt oxide lattice on carbon formation during ethanol decomposition reaction, Appl. Catalysis B: Environ. 254 (2019) 300–311.
[48] A. Ashok, A. Kumar, J. Ponraj, S.A. Mansour, F. Tarlochan, Highly active and stable bi-functional $NiCoO_2$ catalyst for oxygen reduction and oxygen evolution reactions in alkaline medium, Int. J. Hydrogen Energy 44 (2019) 16603–16614.
[49] D. Fa, B. Yu, Y. Miao, Synthesis of ultra-long nanowires of nickel phosphate by a template-free hydrothermal method for electrocatalytic oxidation of glucose, Colloids Surf. Physicochem. Eng. Aspects 564 (2019) 31–38.
[50] J. Huang, W. Qian, H. Ma, H. Zhang, W. Ying, Highly selective production of heavy hydrocarbons over cobalt–graphene–silica nanocomposite catalysts, RSC Adv. 7 (2017) 33441–33449.
[51] A. Ashok, A. Kumar, J. Ponraj, S.A. Mansour, Preparation of mesoporous/microporous $MnCo_2O_4$ and nanocubic $MnCr_2O_4$ using a single step solution combustion synthesis for bifunction oxygen electrocatalysis, J. Electrochem. Soc. 167 (2020), 054507.
[52] B.J. Trzesniewski, O. Diaz-Morales, D.A. Vermaas, A. Longo, W. Bras, M.T. Koper, W.A. Smith, In situ observation of active oxygen species in Fe-containing Ni-based oxygen evolution catalysts: the effect of pH on electrochemical activity, J. Am. Chem. Soc. 137 (2015) 15112–15121.
[53] L. Trotochaud, S.L. Young, J.K. Ranney, S.W. Boettcher, Nickel–iron oxyhydroxide oxygen-evolution electrocatalysts: the role of intentional and incidental iron incorporation, J. Am. Chem. Soc. 136 (2014) 6744–6753.
[54] J. Bao, X. Zhang, B. Fan, J. Zhang, M. Zhou, W. Yang, X. Hu, H. Wang, B. Pan, Y. Xie, Ultrathin spinel-structured nanosheets rich in oxygen deficiencies for enhanced electrocatalytic water oxidation, Angew. Chem. Int. Ed. 54 (2015) 7399–7404.
[55] Y. Zhu, W. Zhou, Y. Chen, J. Yu, X. Xu, C. Su, M.O. Tade, Z. Shao, Boosting oxygen reduction reaction activity of palladium by stabilizing its unusual oxidation states in perovskite, Chem. Mater. 27 (2015) 3048–3054.
[56] Y. Nakayama, F. Soeda, A. Ishitani, XPS study of the carbon fiber matrix interface, Carbon 28 (1990) 21–26.
[57] R. Jansen, H. Van Bekkum, XPS of nitrogen-containing functional groups on activated carbon, Carbon 33 (1995) 1021–1027.
[58] B.J. Matsoso, K. Ranganathan, B.K. Mutuma, T. Lerotholi, G. Jones, N.J. Coville, Time-dependent evolution of the nitrogen configurations in N-doped graphene films, RSC Adv. 6 (2016) 106914–106920.
[59] D. Long, W. Li, L. Ling, J. Miyawaki, I. Mochida, S. Yoon, Preparation of nitrogen-doped graphene sheets by a combined chemical and hydrothermal reduction of graphene oxide, Langmuir 26 (2010) 16096–16102.
[60] Y. Shao, S. Zhang, M.H. Engelhard, G. Li, G. Shao, Y. Wang, J. Liu, I.A. Aksay, Y. Lin, Nitrogen-doped graphene and its electrochemical applications, J. Mater. Chem. 20 (2010) 7491–7496.
[61] J. Li, X. Li, P. Zhao, D.Y. Lei, W. Li, J. Bai, Z. Ren, X. Xu, Searching for magnetism in pyrrolic N-doped graphene synthesized via hydrothermal reaction, Carbon 84 (2015) 460–468.
[62] Y. Chen, B. Xie, Y. Ren, M. Yu, Y. Qu, T. Xie, Y. Zhang, Y. Wu, Designed nitrogen doping of few-layer graphene functionalized by selective oxygenic groups, Nanoscale Res. Lett. 9 (2014) 1–8.
[63] R. Lv, Q. Li, A.R. Botello-Méndez, T. Hayashi, B. Wang, A. Berkdemir, Q. Hao, A.L. Elías, R. Cruz-Silva, H.R. Gutiérrez, Nitrogen-doped graphene: beyond single substitution and enhanced molecular sensing, Sci. Rep. 2 (2012) 586.
[64] D. Yu, Q. Zhang, L. Dai, Highly efficient metal-free growth of nitrogen-doped single-walled carbon nanotubes on plasma-etched substrates for oxygen reduction, J. Am. Chem. Soc. 132 (2010) 15127–15129.
[65] J. Masa, P. Weide, D. Peeters, I. Sinev, W. Xia, Z. Sun, C. Somsen, M. Muhler, W. Schuhmann, Amorphous cobalt boride (Co_2B) as a highly efficient non-precious catalyst for electrochemical water splitting: oxygen and hydrogen evolution, Adv. Energy Mater. 6 (2016) 1502313.
[66] R. Souleymen, Z. Wang, C. Qiao, M. Naveed, C. Cao, Microwave-assisted synthesis of graphene-like cobalt sulfide freestanding sheets as an efficient bifunctional electrocatalyst for overall water splitting, J. Mater. Chem. 6 (2018) 7592–7607.
[67] G. Li, L. Anderson, Y. Chen, M. Pan, P.A. Chuang, New insights into evaluating catalyst activity and stability for oxygen evolution reactions in alkaline media, Sustain. Energy Fuels 2 (2018) 237–251.